Monthly Notices
of the
ROYAL ASTRONOMICAL SOCIETY

MNRAS **477,** 957–963 (2018) doi:10.1093/mnras/sty744

Twin radio relics in the nearby low-mass galaxy cluster Abell 168

K. S. Dwarakanath,[1]★ V. Parekh,[1] R. Kale[2]★ and L. T. George[1]

[1]*Raman Research Institute, C V Raman Av, Sadashivanagar, Bangalore 560080, India*
[2]*National Center for Radio Astrophysics, Tata Institute of Fundamental Research, Post Bag 3, Pune 411007, India*

Accepted 2018 March 10. Received 2018 March 2; in original form 2017 December 22

ABSTRACT

We report the discovery of twin radio relics in the outskirts of the low-mass merging galaxy cluster Abell 168 (redshift=0.045). One of the relics is elongated with a linear extent ∼800 kpc and projected width of ∼80 kpc and is located ∼900 kpc towards the north of the cluster centre, oriented roughly perpendicular to the major axis of the X-ray emission. The second relic is ring-shaped with a size ∼220 kpc and is located near the inner edge of the elongated relic at a distance of ∼600 kpc from the cluster centre. These radio sources were imaged at 323 and 608 MHz with the Giant Meterwave Radio Telescope and at 1520 MHz with the Karl G. Jansky Very Large Array (VLA). The elongated relic was detected at all frequencies, with a radio power of $1.38 \pm 0.14 \times 10^{23}$ W Hz^{-1} at 1.4 GHz and a power law in the frequency range 70–1500 MHz ($S \propto \nu^{\alpha}$, $\alpha = -1.1 \pm 0.04$). This radio power is in good agreement with that expected from the known empirical relation between the radio powers of relics and host cluster masses. This is the lowest mass ($M_{500} = 1.24 \times 10^{14}\, M_{\odot}$) cluster in which relics due to merger shocks are detected. The ring-shaped relic has a steeper spectral index (α) of -1.74 ± 0.29 in the frequency range 100–600 MHz. We propose this relic to be an old plasma, revived due to adiabatic compression by the outgoing shock that produced the elongated relic.

Key words: radiation mechanisms: non-thermal – techniques: interferometric – galaxies: clusters: individual: A168 – galaxies: clusters: intracluster medium – radio continuum: general – X-rays: galaxies: clusters.

1 INTRODUCTION

Diffuse radio emission in galaxy clusters can be broadly classified into two categories: haloes and relics, respectively found predominantly in the central regions and towards the peripheries of clusters. Neither of them is associated with the currently active galaxies of clusters. Haloes are typically of ∼1 Mpc extent, with a roundish morphology and low surface brightness (∼1 mJy arcmin^{-2} at 1.4 GHz), and are unpolarized to a level of a few per cent. Haloes tend to have steep radio spectra with $\alpha < -1$, where $S \propto \nu^{\alpha}$, S being the flux density. Relics are similar to haloes in terms of their extent in one direction, with narrow (∼0.1 Mpc) extent in the perpendicular direction. Relics have somewhat higher surface brightnesses, but have similar spectra to haloes. However, they are located towards the cluster periphery (∼1 Mpc from the cluster centre) and are polarized to an extent of ∼20 per cent (Feretti et al. 2012; Brunetti & Jones 2014). About 30 per cent of high X-ray luminosity ($L_{\rm x} > 5 \times 10^{44}$ erg s^{-1}) clusters host radio haloes and relics. A positive correlation between the radio powers of haloes and relics at 1.4 GHz and the X-ray luminosities of respective host clusters has been observed (Feretti et al. 2012).

The radio emission from haloes and relics is known to be synchrotron in origin, with ∼GeV electrons radiating in ∼μG magnetic fields in clusters. The most important puzzle as regards the existence of such diffuse radio emission in galaxy clusters has been their extents. The diffusion time-scales of relativistic electrons needed to cover these extents are more than 10 times larger than the lifetimes of the radiating electrons at a frequency ∼1 GHz (Jaffe 1977). One of the ways to get around this problem is to postulate *in situ* acceleration of relativistic electrons, thus avoiding the time-scale problem. Magnetic fields have been found to be ubiquitous in galaxy clusters (Carilli & Taylor 2002).

Cluster-wide turbulence is believed to be responsible for *in situ* acceleration of relativistic electrons that produce radio haloes. Cluster mergers have been invoked to create turbulence in the cluster volume. Mildly relativistic seed electrons present in the cluster volume (from previous active galactic nucleus (AGN) activities, for example) are believed to be accelerated to relativistic energies through their interactions with turbulence. Turbulent acceleration is inefficient and short-lived, as a consequence of which the halo emission is believed to be correlated with recent merger activities of clusters. Indeed, a correlation between the dynamical states of clusters and the existence of radio haloes and relics in them has been observed, with haloes and relics being found predominantly in non-virialized clusters (Brunetti et al. 2007, 2009; Cassano et al. 2010; Donnert et al. 2013).

★ E-mail: dwaraka@rri.res.in (KSD); ruta@ncra.tifr.res.in (RK)

At least two types of radio relic are known to exist in clusters. Large (∼ Mpc) relics are found towards the peripheries of clusters, oriented perpendicular to the merger axes of clusters (Bagchi et al. 2006; van Weeren et al. 2010, 2012). These relics are produced by outgoing merger shocks. While the overall mechanism for producing relativistic electrons is believed to be diffusive shock acceleration at the sites of these shocks, the seed electrons can come from both the thermal pool of electrons and the mildly relativistic fossil electrons left over from earlier AGN activities (Ensslin et al. 1998; Markevitch et al. 2005). Cluster merger simulations have been carried out to account for the occurrence of relics and their properties. Some of the basic properties of relics, like their morphology, spectral index variations from the shock edge towards the post-shock regions and steepening of the spectral index at higher frequencies, have been accounted for to some extent (Enßlin & Brüggen 2002; Kang & Ryu 2015; Kang 2017). A recent example of re-acceleration of electrons by shocks in galaxy clusters has been found in Abell 3411–3412 (van Weeren et al. 2017). The second type of relic is the radio 'phoenix', which is believed to trace the compressed fossil plasma. Such 'phoenices' are found in both central and peripheral regions of clusters and display steep and curved spectra (Slee et al. 2001; Enßlin & Gopal-Krishna 2001; Enßlin & Brüggen 2002; Kale & Dwarakanath 2012).

The diffuse radio emission associated with the galaxy cluster Abell 168 (hereafter A168) was discovered in cross-referencing of the Meta-Catalogue of X-ray detected Clusters (MCXC) of galaxies with the GaLactic and Extragalactic All-sky MWA (GLEAM) survey at 200 MHz carried out by the Murchison Widefield Array (MWA: Hurley-Walker et al. 2017) . The MCXC is a catalogue of X-ray-detected galaxy clusters based on the publicly available *ROSAT* All-Sky Survey and serendipitous discoveries (Piffaretti et al. 2011). This catalogue consists of a total of 1743 galaxy clusters with homogenized properties such as redshift, 0.1–2.4 keV band luminosity L_{500}, total mass M_{500} and radius R_{500} available for each cluster. The GLEAM survey covers the entire sky south of $\delta = +30^{\circ}$ in the frequency range 72–231 MHz. The instantaneous frequency coverage of the MWA is 30.72 MHz and hence the above-mentioned frequency range is divided into five bands, providing near-contiguous coverage. In addition, this survey also produced images at 200 MHz with a bandwidth of 60 MHz, resulting in a resolution of ∼2 arcmin and a sensitivity of ∼5 mJy beam^{-1}. The diffuse radio emission in A168 was also detected as part of the project to catalogue all diffuse radio sources in clusters using the GLEAM survey (M. Johnston-Hollitt, private communication). An overlay of the GLEAM 200-MHz image on the *XMM-Newton* image of the A168 cluster is shown in Fig. 1. Some basic properties of A168 are given in Table 1. A168 is also detected in the *Planck* observations (PSZ2 G135.76-62.03) and its Sunyaev–Zel'dovich (SZ) mass is $\sim 1.52 \times 10^{14}$ M$_{\odot}$ (Planck Collaboration XXVII 2016).

The cosmology used in this article is $H_0 = 70\,\mathrm{km\,s^{-1}\,Mpc^{-1}}$, $\Omega_{\mathrm{M}} = 0.3$ and $\Omega_{\Lambda} = 0.7$, giving a luminosity distance of 199.3 Mpc to A168 with an assumed redshift of 0.045.

2 OBSERVATIONS

2.1 GMRT observations

The cluster A168 was observed with the Giant Meterwave Radio Telescope (GMRT) in the standard 325- and 610-MHz bands during 2016 November 26–27. A continuous track of 8 h was carried out at each of the two centre frequencies, with a bandwidth of 32 MHz and 512 channels. The GMRT Software Backend was used for these observations. Primary calibrators 3C48 and 3C147 were used, along with the secondary gain calibrator 0059+001 at both frequencies.

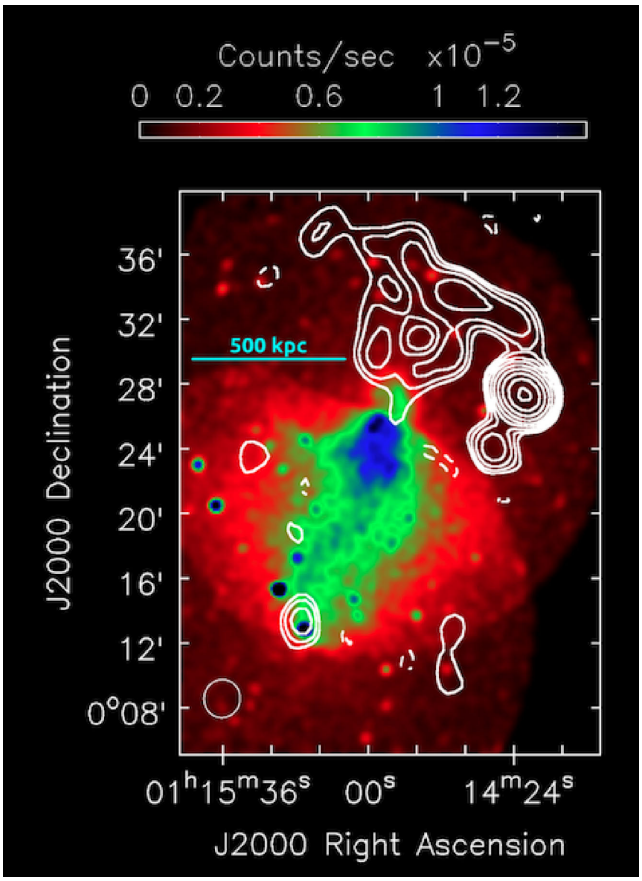

Figure 1. Radio image at 200 MHz (contours) from the wide-band (170–231 MHz) GLEAM survey made using the MWA overlaid on the *XMM-Newton* X-ray image. The radio image has a synthesized beam of 141×134 arcsec^2, -10° with an RMS (σ) of 9 mJy beam^{-1}. The first contour is at 3σ and contours increase in steps of $\sqrt{2}$. Dashed lines indicate negative contours.

2.2 VLA observations

Karl G. Jansky Very Large Array (VLA) observations of A168 were carried out on 2017 April 28, when the array was in the D configuration (maximum baseline ∼1 km). The total observing time was ∼2.5 h. The observations were carried out in the frequency range 1–2 GHz with 16 spectral windows, each spectral window having 64 channels. The primary and secondary calibrators used were 3C138 and J0059+0006, respectively.

3 DATA ANALYSIS

3.1 VLA data analysis

To analyse the VLA data, the Very Large Array calibration pipeline, which performs basic flagging and calibration, was used.[1] The shortest baseline from which data were available was 200λ, with the longest baseline available being ∼5000λ (∼1 km). This calibrated data was analysed further using the Common Astronomy Software

[1] https://science.nrao.edu/facilities/vla/data-processing/pipeline

Table 1. X-ray properties.

Cluster	RA (J2000)			Dec. (J2000)			z	L_X (0.1–2.4 keV)	M_{SZ}
	hh	mm	ss	°	′	″		(10^{44} erg s^{-1})	(10^{14} M$_\odot$)
A168	01	15	12.0	+00	19	48	0.0450	0.46	1.52

Applications (CASA) package (McMullin et al. 2007). The imaging was carried out using the multi-scale, multi-frequency synthesis method in the task CLEAN, which takes into account the large bandwidth used in these observations, in addition to recovering the extended emission as well as possible. Furthermore, imaging was also carried out taking into account the spectral curvature across the band (Taylor terms = 2 in the task CLEAN) and the wide field of view (w-projection in the task CLEAN: Cornwell, Golap & Bhatnagar 2008; Rau & Cornwell 2011). A suitable number of phase and amplitude self-calibrations were carried out to obtain the best images, as evidenced by minimum root-mean-square value (RMS) and least systematics.

Images of different resolutions and sensitivities were produced by varying the weighting of the visibilities (robust parameter in the task CLEAN). Varying the robust parameter (Briggs 1995) from −2 to +2 changes the weighting of the visibilities from 'uniform' to 'natural'. Natural weighting produces images sensitive to extended emission, but with a loss of resolution. Uniform weighting, on the other hand, produces images with the best resolution but at the loss of sensitivity to extended emission. The final image adopted here is the one produced with robust = 1, which is a compromise between sensitivity to extended emission and resolution.

3.2 GMRT data analysis

The GMRT observations were analysed using the Source Peeling And Modelling (SPAM) package (Intema et al. 2009). SPAM is an Astronomical Image Processing Software (AIPS)-based Python package that provides semi-automated data reduction scripts for all sub-GHz frequencies at GMRT (Intema 2014). Apart from incorporating well-tested data reduction steps like calibration, wide-field imaging and self-calibration, SPAM also incorporates direction-dependent gain calibration and imaging and radio-frequency interference excision methods (Intema 2014). Images of the A168 field were produced with different weightings, tapers and uv ranges of visibilities included in the imaging. The GMRT observations were also analysed using AIPS and the images produced by these two methods were compared. There was excellent agreement between the two sets of images.

The shortest baseline included in the imaging at 323 and 608 MHz was 200λ, to be consistent with the VLA observations. This restriction also excludes some of the shortest baseline visibilities from GMRT, which are invariably corrupted by radio-frequency interference. The final images used here are the ones with a value of robust = 1 in the imaging task CLEAN, for reasons already explained. Since the VLA observations were carried out in the D configuration (maximum baseline ∼1 km), the higher resolution observations at 323 and 608 MHz from GMRT (maximum baseline ∼25 km) were imaged to have the same resolutions as those from the VLA observations, by suitable tapering of the visibilities. All the images were corrected for the respective primary beam attenuations. The higher resolution GMRT observations were examined for possible unresolved sources contaminating the cluster diffuse emission.

3.3 Flux density scale

The GLEAM survey is on the flux density scale of Baars et al. (1977) and is accurate to ∼8 per cent. The GMRT flux densities are on the Scaife & Heald (2012) scale. These two scales are in agreement to within 3 per cent (Hurley-Walker et al. 2017). The VLA flux densities are tied to the Perley & Butler (2017) flux density scale, which is in agreement with the Scaife & Heald (2012) scale to within 5 per cent.

4 RESULTS

An image at 323 MHz from GMRT is overlaid on the GLEAM 200 MHz image in Fig. 2(a). In Fig. 2(b) the above GMRT 323-MHz image is shown convolved to the same resolution as the GLEAM 200-MHz image. In Fig. 2(c) the 323-MHz image at a resolution of 25 arcsec is overlaid on the GMRT 608-MHz image at the same resolution. In Fig. 2(d), a 323-MHz image at a resolution of 52 arcsec resolution is overlaid on the VLA 1520-MHz image.

The diffuse emission detected in the GLEAM survey can be discussed as two sources A and B, as marked in Fig. 2(a). Source B refers to the northern source, while source A refers to the southern ring-shaped region. Source B is detected in all the images shown here, while source A is detected at all except the VLA images. The estimated flux densities of extended sources A and B from these images are given in Table 2. There are two primary sources of errors in the estimation of the flux densities of extended sources. First, there is an error due to uncertainties in the flux densities of the primary and secondary calibrators at different frequencies. This error is estimated to be ∼10 per cent. Secondly, the errors in the flux-density estimates of extended sources will be the RMS in the image (Table 2) multiplied by the square root of the ratio of the solid angle of the extended source to that of the synthesized beam. Since these two sources of errors are unrelated, they are added in quadrature to estimate the total error in the flux densities of the extended sources (given in parantheses in Table 2).

There are no flux-density estimates of sources A and B corresponding to the GLEAM survey frequencies at 87.5 and 118 MHz. This is because sources A and B are convolved into one source at these frequencies, due to poorer resolution. However, the sum of the extrapolated flux densities of sources A and B at 118 MHz is in agreement, within the errors of the observed flux density of the convolved source at 118 MHz. The flux density estimate at 74 MHz is from the VLSSr survey at a resolution of ∼80 arcsec (Lane et al. 2014), convolved to the same resolution as the GLEAM survey images at 200 MHz. The measured flux density from VLSSr was scaled down by a factor of 1.1 to be consistent with the Baars et al. scale used here (Lane et al. 2014). The flux densities of sources E (S_{323} = 7.7 mJy, $\alpha = -0.89$) and F (S_{323} = 5.4 mJy, $\alpha = -0.8$), which are unrelated to diffuse source B but are convolved into source B at poorer resolutions, are subtracted from the estimated flux densities of source B. In any case, the total flux density of sources E and F is less than 10 per cent of that of source B at 323 MHz. Optical

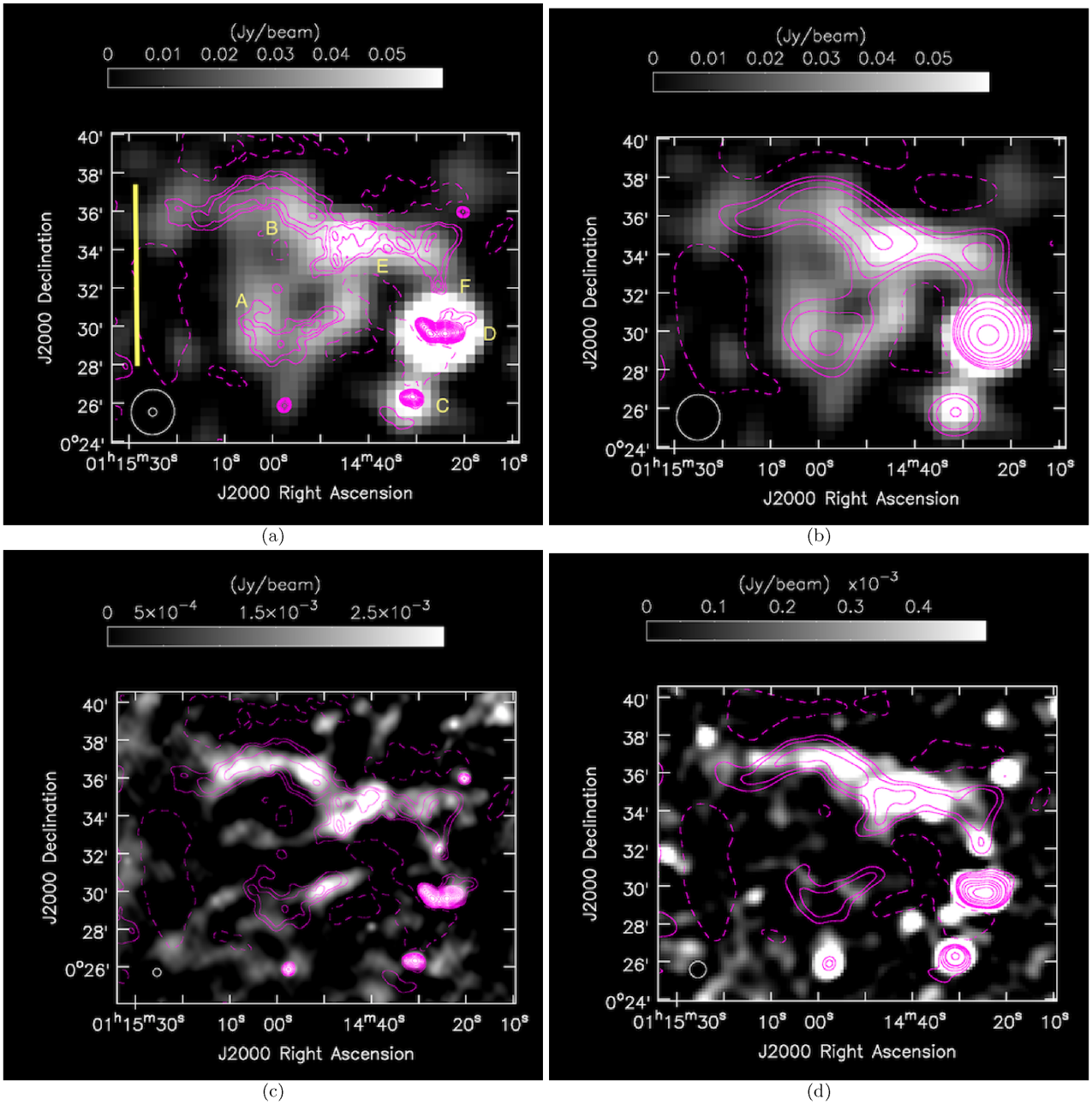

Figure 2. A168. (a) GMRT 323-MHz image (contours) (25×25 arcsec^2, $\sigma = 1.0$ mJy beam^{-1}) overlaid on the GLEAM 200-MHz image (grey-scale). The vertical line indicates 500 kpc. (b) GMRT 323-MHz image convolved to the same resolution (contours, $\sigma = 15.4$ mJy beam^{-1}) as the GLEAM 200-MHz image and overlaid on the GLEAM 200-MHz image (grey-scale). (c) GMRT 323-MHz contours overlaid on the GMRT 608-MHz grey-scale image ($\sigma = 0.64$ mJy beam^{-1}). Both images are at a resolution of 25×25 arcsec^2. (d) GMRT 323-MHz contours ($\sigma = 4.2$ mJy beam^{-1}) overlaid on the VLA image at 1520 MHz (grey-scale, $\sigma = 160$ μJy beam^{-1}). Both images are at a resolution of 52×52 arcsec^2. In all the images, the first contour is drawn at 2σ. Contour levels increase in steps of $\sqrt{2}$. Dashed lines indicate negative contours. The synthesized beams are indicated in the bottom left hand corner.

Table 2. Flux densities of sources A and B. The data used are from VLSSr (74 MHz, Lane et al. 2014), the GLEAM survey (154 and 200 MHz) and the present work (323, 608 and 1520 MHz). The 74-MHz image at a resolution of 80 arcsec^2 was convolved to the GLEAM survey resolution at 200 MHz. The integrated flux densities of sources A and B are given in mJy. The values in parantheses are total errors in the flux densities, estimated as described in the text. The upper limits are 3σ values.

Frequency (MHz)	74	154	200	323	608	1520
Synthesized beam (arcsec^2, $^\circ$)	$141 \times 134, -10$	$173 \times 163, -10$	$141 \times 134, -10$	52×52	52×52	52×52
RMS (mJy beam^{-1})	200	13.7	8.2	4.2	2.0	0.16
A	<600	339(36.6)	149(19.3)	96(15.8)	28(6.6)	<0.48
B	864(200)	348(43)	222(32)	155(29.5)	66(13.0)	28(3.0)

Table 3. Discrete sources. In the case of source D, the two radio positions correspond to the peaks of emission of the two lobes, respectively. The optical position corresponds to that of the core between the two lobes.

Source	Identification	Optical						z	mag	Radio						Separation
		RA (J2000)			Dec. (J2000)					RA (J2000)			Dec. (J2000)			
		hh	mm	ss	°	′	″			hh	mm	ss	°	′	″	″
C	SDSS J011431.02+002621.4	01	14	31.0	+00	26	21	1.76	–	01	14	31.00	00	26	19.60	1.8
D	SDSS J011425.58+002932.7	01	14	25.6	+00	29	33	0.35	20.4g	01	14	27.00	00	29	39.59	
										01	14	24.17	00	29	39.59	
E	SDSS J011435.83+003356.9	01	14	35.8	+00	33	57	0.54	21.3g	01	14	35.67	00	33	59.60	3.5
F	CGCG385–039	01	14	25.7	+00	32	10	0.04	15.5g	01	14	25.50	00	32	09.58	2.6

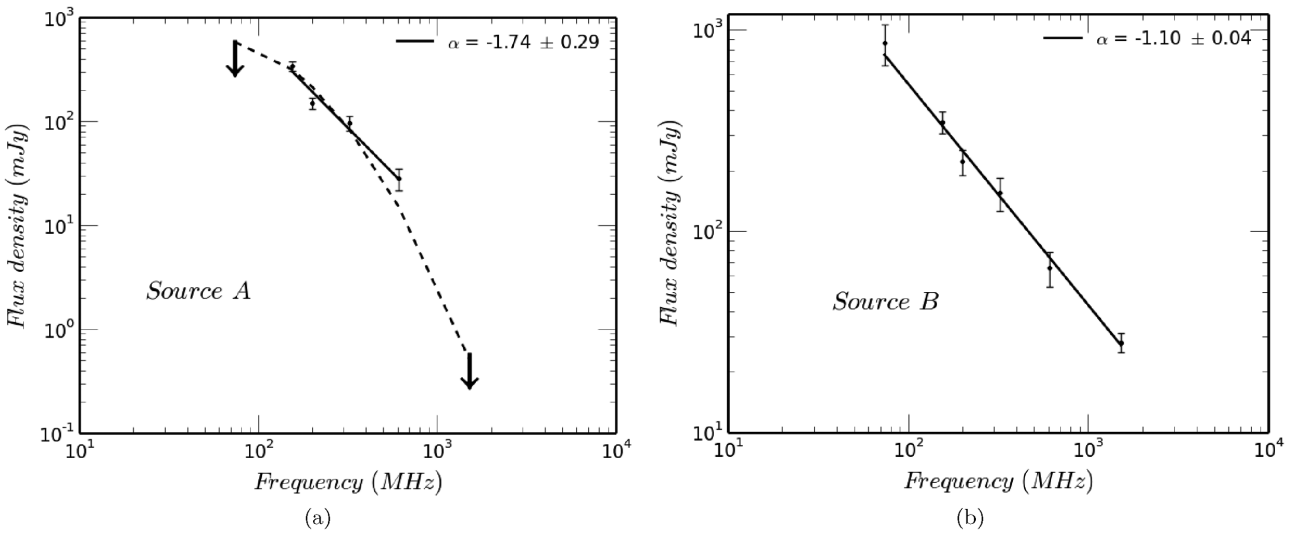

Figure 3. Spectra of relics. A linear fit to the four data points for source A gives $\chi^2_{\rm red} = 2.8$ (DOF=2), with the slope indicated in the top right-hand corner of this panel. Given the upper limit at 1.5 GHz, the spectrum of source A is likely to be an exponentially falling spectrum at higher frequencies, as indicated by the broken lines. The best-fitting power law to the source B spectrum gives $\chi^2_{\rm red} = 0.4$ (DOF=4), with the slope indicated in the top right-hand corner. The error bars correspond to total errors estimated as described in the text.

identifications for sources C–F are given in Table 3. The spectra of sources A and B are given in Fig. 3.

5 DISCUSSION

There are four discrete sources, C, D, E and F, which are near (in projection) to the diffuse sources A and B. As can be seen from Table 3, source D is a double radio galaxy with an optical counterpart ($z = 0.35$) in between the lobes where the core is presumably situated. Sources C and E are background sources at redshifts of 1.76 and 0.54, respectively. Source F is a cluster member. In the absence of any possible jet connecting this source to sources A and B, source F does not appear related to them. Furthermore, the region of the sky covering sources A and B was also searched for any optical and infrared sources (with or without redshift measurements) that could possibly have supplied fossil plasma, particularly for source A. No such source was detected.

The elongated (length ∼800 kpc) source B is located towards the cluster periphery at a distance ∼700 kpc from the X-ray peak and ∼900 kpc from the cluster centre. The thickness of the relic is ∼80 kpc and the orientation of the longer dimension of the relic is nearly perpendicular to the major axis of X-ray emission (Fig. 1). The morphology and the location of relic B are not unlike those of the well-known 'sausage' and 'toothbrush' relics found in galaxy clusters (van Weeren et al. 2010, 2012). The spectral index of the relic in the frequency range 70–1500 MHz is steep ($\alpha = -1.08$, Fig. 3b) but well within the known distribution of spectral indices of relics ($\alpha = -1.42 \pm 0.37$, Feretti et al. 2012). Relic A, on the other hand, has a roundish or ring-shaped morphology. With an extent of ∼220 kpc, it is located closer to the X-ray peak at a distance of ∼400 kpc. The spectrum of relic A appears curved, with an exponential cut-off towards higher frequencies and a flattening towards lower frequencies (Fig. 3a). The best-fitting power law for the four detections between 150 and 608 MHz implies a spectral index of -1.70 ± 0.15 (Fig. 3a).

5.1 Cluster dynamics and relics

The role of cluster mergers in producing shocks underlying radio relics at cluster peripheries is well supported by observational evidence (Giovannini, Tordi & Feretti 1999; Bagchi et al. 2006; van Weeren et al. 2009; Venturi et al. 2013). A different class of relics, proposed to be fading radio galaxy lobes or such lobes revived due to adiabatic compression (Enßlin & Gopal-Krishna 2001), are also well known to occur in clusters. Examples of relics in this category are those in Abell 4038 (Slee & Roy 1998; Kale & Dwarakanath 2012) and Abell 85 (Slee et al. 2001). In A168 we find an arc-like relic at the periphery (B) and a smaller steep-spectrum relic (A) in its wake, as seen projected in the plane of the sky. The intracluster medium (ICM) in the cluster is elongated along the north–south direction and the orientation of B is perpendicular to this direction. Merger-shock-related relics have been found to be

oriented preferentially perpendicular to the elongation axis of the ICM (van Weeren et al. 2011). The flat spectral index of B, arc-like morphology and orientation thus support the scenario that a cluster merger along the north–south direction led to an outgoing merger shock that accelerated electrons, which are detected as relic B. Relic A has a steep and curved spectrum (Fig. 3) indicative of an ageing population of relativistic electrons. We propose that relic A is a candidate adiabatically compressed lobe of a radio galaxy, the compression having been caused by the outgoing shock at B. Simulations of adiabatically compressed cocoons of radio galaxies have shown that, as compression proceeds, the cocoon is torn into filamentary structures, which can appear like a single torus or multiple tori at late stages (Enßlin & Brüggen 2002). The morphology of relic A is complex and filamentary, which compares well with the predicted structures of compressed cocoons. The morphology of B is not smooth at the outer boundary, but shows kink-like features connected to A, implying a possible distortion due to the presence of a radio cocoon in the path of the outgoing shock that led to the formation of A.

There is evidence for a binary merger along the north–south direction in A168 based on optical and X-ray observations. Yang et al. (2004) have estimated a merger time-scale of 0.6 Gyr assuming the distance between two X-ray peaks to be 676 kpc and a colliding velocity of 600 km s^{-1}. For relic A, if the break frequency is considered to be at ∼100 MHz and the magnetic field is assumed to be 1 μG, typical of the cluster outskirts (Feretti et al. 2012), the lifetime due to synchrotron and inverse Compton losses is ∼0.24 Gyr. Since the initial age of the radio cocoon that may have formed A is unknown, the estimated age of A could be considered a minimum. The time taken by a shock with a speed of 600 km s^{-1} to traverse from A to B, which is a distance of ∼320 kpc, is 0.5 Gyr. These time-scales are comparable with the minimum estimated merger time-scale, making the proposed scenario plausible.

Measurement of polarization in relics A and B will provide further evidence for the passage of a shock. Deep X-ray observations towards the relics are also needed to detect the location and strength of the underlying shock.

5.2 Implications of the low-mass host cluster

Mergers in massive systems are favoured sites for turbulent re-acceleration of particles, leading to radio haloes, and shocks, leading to radio relics (e.g. Cuciti et al. 2015). Radio haloes in low-mass systems ($M < 5 \times 10^{14}$ M$_\odot$) are not common, but radio relics have been found in low-mass systems (de Gasperin et al. 2017; Kale et al. 2017). We show the radio relic power ($P_{1.4\,\mathrm{GHz}}$) versus host cluster mass scaling, with relic B in A168 plotted (Fig. 4). A168 is the lowest mass system so far known to have radio relics of merger shock origin. The physical mechanism behind the observed empirical relation between $P_{1.4\,\mathrm{GHz}}$ and the host cluster mass is not well understood (de Gasperin et al. 2014). The sample of single relics shows a large scatter around the scaling; however, A168 relic B lies close to the radio power expected according to the scaling relation. A counter-relic in A168 may be present, but is not detected in our observations. Such counter-relics have been found to be factors of 8 or so weaker (e.g. A3365: van Weeren et al. (2011)) and thus may not be detectable. The physical mechanism behind the observed empirical scaling is not known and relic B in A168 extends this scaling to even lower masses. This indicates that not only the cluster mass but also other factors, such as the availability of seed electrons, strength of the magnetic field and merger geometry itself, may play a role in producing radio relics of certain radio powers.

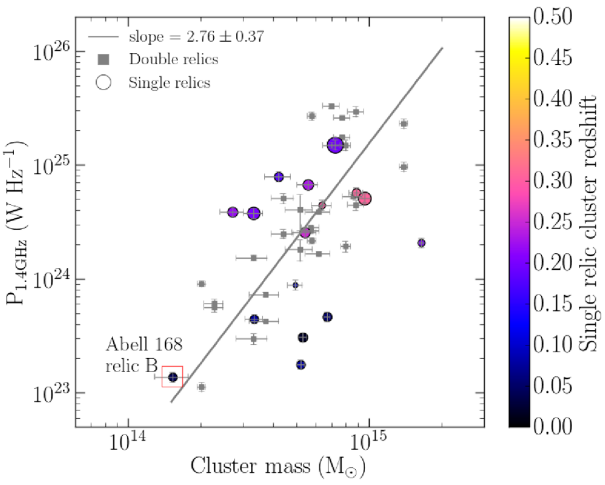

Figure 4. The radio relic powers at 1.4 GHz versus the host cluster masses for a sample of double and single relics taken from (Kale et al. 2017). The grey filled squares are the double relics for which the best-fitting line is shown (de Gasperin et al. 2014). Single relics are shown by circles filled with colour, indicating the redshift and size scaled with the relic linear size. The A168 single relic (source B) is highlighted with a square. It is the lowest mass cluster known to date with a candidate shock-related single relic.

6 SUMMARY AND CONCLUSIONS

We report the detection of twin radio relics in the low-mass galaxy cluster A168. These relics were discovered in a cross-referencing of the MCXC catalogue with the GLEAM survey. We have imaged these relics at 230 and 610 MHz using the GMRT and at 1520 MHz using the VLA. One of the relics (B) is elongated (∼800 kpc), thin (∼80 kpc) and located towards the northern periphery of the cluster at a distance of ∼900 kpc from the cluster centre. The second relic (A) is ring-shaped, with an extent of ∼220 kpc, and is located near the inner edge of B. Relic B was detected at all the observed frequencies with a radio power at 1.4 GHz of $1.38 \pm 0.14 \times 10^{23}$ W Hz^{-1}, having a power law in the frequency range 70–1500 MHz ($S \propto \nu^{\alpha}$, $\alpha = -1.08 \pm 0.04$). This radio power is in good agreement with that expected from the known empirical relation between radio powers of relics and host cluster masses, with the current relic detection from the lowest mass ($M_{500} = 1.24 \times 10^{14} M_\odot$) cluster. Relic A has a steeper spectral index (α) of -1.70 ± 0.15 in the frequency range 100–600 MHz and appears connected to source B. We propose source A to be an old plasma, revived due to adiabatic compression by the outgoing shock that produced source B. The orientation of source B, the projected distance between sources A and B and the radiative lifetime of source A are consistent with such a scenario. Polarization measurements of sources A and B and deeper X-ray observations at the positions of sources A and B will be needed to detect the underlying shock.

ACKNOWLEDGEMENTS

We thank Huib Intema for useful discussions on using SPAM. We thank the referee for a critical reading of the manuscript and constructive criticisms. We thank the staff of the GMRT, who made these observations possible. GMRT is run by the National Centre for Radio Astrophysics of the Tata Institute of Fundamental Research. The National Radio Astronomy Observatory is a facility of the National Science Foundation operated under cooperative agreement by Associated Universities, Inc.

REFERENCES

Baars J. W. M., Genzel R., Pauliny-Toth I. I. K., Witzel A., 1977, A&A, 61, 99

Bagchi J., Durret F., Neto G. B. L., Paul S., 2006, Sci, 314, 791

Briggs D. S., 1995, BAAS, 27, 1444

Brunetti G., Jones T. W., 2014, Int. J. Mod. Phys. D, 23, 30007

Brunetti G., Venturi T., Dallacasa D., Cassano R., Dolag K., Giacintucci S., Setti G., 2007, ApJ, 670, L5

Brunetti G., Cassano R., Dolag K., Setti G., 2009, A&A, 507, 661

Carilli C. L., Taylor G. B., 2002, ARA&A, 40, 319

Cassano R., Ettori S., Giacintucci S., Brunetti G., Markevitch M., Venturi T., Gitti M., 2010, ApJ, 721, L82

Cornwell T. J., Golap K., Bhatnagar S., 2008, IEEE Journal of Selected Topics in Signal Processing, 2, 647

Cuciti V., Cassano R., Brunetti G., Dallacasa D., Kale R., Ettori S., Venturi T., 2015, A&A, 580, A97

de Gasperin F., van Weeren R. J., Brüggen M., Vazza F., Bonafede A., Intema H. T., 2014, MNRAS, 444, 3130

de Gasperin F. et al., 2017, A&A, 597, A15

Donnert J., Dolag K., Brunetti G., Cassano R., 2013, MNRAS, 429, 3564

Enßlin T. A., Brüggen M., 2002, MNRAS, 331, 1011

Enßlin T. A., Gopal-Krishna, 2001, A&A, 366, 26

Ensslin T. A., Biermann P. L., Klein U., Kohle S., 1998, A&A, 332, 395

Feretti L., Giovannini G., Govoni F., Murgia M., 2012, A&AR, 20, 54

Giovannini G., Tordi M., Feretti L., 1999, New Astron., 4, 141

Hurley-Walker N. et al., 2017, MNRAS, 464, 1146

Intema H. T., 2014, in Chengalur J. N., Gupta Y., eds., ASI Conf. Ser. Vol. 13, The Metrewavelength Sky, p. 469

Intema H. T., van der Tol S., Cotton W. D., Cohen A. S., van Bemmel I. M., Röttgering H. J. A., 2009, A&A, 501, 1185

Jaffe W. J., 1977, ApJ, 212, 1

Kale R., Dwarakanath K. S., 2012, ApJ, 744, 46

Kale R., Wik D. R., Giacintucci S., Venturi T., Brunetti G., Cassano R., Dallacasa D., de Gasperin F., 2017, MNRAS, 472, 940

Kang H., 2017, J. Korean Astron. Soc., 50, 93

Kang H., Ryu D., 2015, IAU General Assembly, 22, 2227971

Lane W. M., Cotton W. D., van Velzen S., Clarke T. E., Kassim N. E., Helmboldt J. F., Lazio T. J. W., Cohen A. S., 2014, MNRAS, 440, 327

Markevitch M., Govoni F., Brunetti G., Jerius D., 2005, ApJ, 627, 733

McMullin J. P., Waters B., Schiebel D., Young W., Golap K., 2007, in Shaw R. A., Hill F., Bell D. J., eds, ASP Conf. Ser. Vol. 376, Astronomical Data Analysis Software and Systems XVI. Astron. Soc. Pac., San Francisco, p. 127

Perley R. A., Butler B. J., 2017, ApJS, 230, 7

Piffaretti R., Arnaud M., Pratt G. W., Pointecouteau E., Melin J.-B., 2011, A&A, 534, A109

Planck Collaboration XXVII, 2016, A&A, 594, A27

Rau U., Cornwell T. J., 2011, A&A, 532, A71

Scaife A. M. M., Heald G. H., 2012, MNRAS, 423, L30

Slee O. B., Roy A. L., 1998, MNRAS, 297, L86

Slee O. B., Roy A. L., Murgia M., Andernach H., Ehle M., 2001, AJ, 122, 1172

van Weeren R. J. et al., 2009, A&A, 506, 1083

van Weeren R. J., Röttgering H. J. A., Brüggen M., Hoeft M., 2010, Science, 330, 347

van Weeren R. J., Brüggen M., Röttgering H. J. A., Hoeft M., Nuza S. E., Intema H. T., 2011, A&A, 533, A35

van Weeren R. J., Röttgering H. J. A., Intema H. T., Rudnick L., Brüggen M., Hoeft M., Oonk J. B. R., 2012, A&A, 546, A124

van Weeren R. J. et al., 2017, Nature Astron., 1, 0005

Venturi T., Giacintucci S., Dallacasa D., Cassano R., Brunetti G., Macario G., Athreya R., 2013, A&A, 551, A24

Yang Y., Huo Z., Zhou X., Xue S., Mao S., Ma J., Chen J., 2004, ApJ, 614, 692

This paper has been typeset from a TEX/LATEX file prepared by the author.